PCCP

ARTICLE TYPE

Cite this: DOI: 00.0000/xxxxxxxxxx

On the role of dynamic electron correlation in non-orthogonal configuration interaction with fragments†

A. Sánchez-Mansilla,[a] C. Sousa,*[b] R. K. Kathir,¶[c] R. Broer,[c] T. P. Straatsma,[d,e] and C. de Graaf*[a,c,f]

Received Date
Accepted Date

DOI: 00.0000/xxxxxxxxxx

Two different approaches have been implemented to include the effect of dynamic electron correlation in the Non-Orthogonal Configuration Interaction for Fragments (NOCI-F) method. The first is based on shifting the diagonal matrix elements of the NOCI matrix, while the second incorporates the dynamic correlation explicitly in the fragment wave functions used to construct the many-electron basis functions of the NOCI. The two approaches are illustrated for the calculation of the electronic coupling relevant in singlet fission and the coupling of spin moments in organic radicals. Comparison of the calculated diabatic couplings, the NOCI energies and wave functions shows that dynamic electron correlation is not only efficiently but also effectively incorporated by the shifting approach and can largely affect the coupling between electronic states. Also, it brings the NOCI coupling of the spin moments in close agreement with benchmark calculations.

1 Introduction

The strength of the coupling between electronic states dominated by different electronic configurations plays a key role in the interpretation of some highly interesting phenomena such as multiple exciton generation (in particular singlet fission),[1,2] intermolecular Coulombic decay,[3] exciton diffusion,[4] and electron transfer in donor-acceptor systems. Similarly, the coupling of spin moments in compounds with organic radicals or transition or rare-earth metal ions gives also rise to fascinating physics such as single-molecule-magnet behaviour[5,6] and colossal magnetoresistance.[7,8].

In both cases, accurate estimates of the couplings can be helpful to understand, control and improve such processes. The coupling between different electronic states is not an observable, and hence, 'experimental' information has to rely on indirect measurements in combination with phenomenological models. The coupling among spin moments can in many cases accurately be estimated from experimental data, but an adequate model of the topology is required to guide the parameter extraction, otherwise erroneous conclusions about the coupling can be obtained.[9,10] From a theoretical viewpoint, the coupling between two electronic states depends on the matrix elements of the hamiltonian expressed in the basis of the diabatic representation of the electronic states of interest. The spin moment coupling is directly related to the energy difference of the electronic states with different total spin moment.[11,12] Hence, theory (and more specifically computations) can make an important contribution to understanding and controlling the couplings and eventually improve the materials that show the above-mentioned physics.

There are multiple computational approaches for efficient calculation of the coupling between electronic states ranging from simple one-electron models using only the HOMO and LUMO energies[13] to estimates based on multiconfigurational wave function approaches. In between there is a whole spectrum of other methods using constrained density functional theory (C-DFT),[14], Restricted active space spin-flip (RAS-SF),[15,16] equation-of-motion coupled-cluster (EOM-CC),[17–19] truncated configuration interactions[20] and other approaches, such as the generalized Mulliken-Hush scheme, that use auxiliary operators to define initial and final electronic states,[21] for example local transition dipole moments.[22,23]

[a] Departament de Química Física i Inorgànica, Universitat Rovira i Virgili, Tarragona, Spain.
[b] Departament de Ciència de Materials i Química Física and Institut de Química Teòrica i Computacional, Universitat de Barcelona, Spain; E-mail: csousa@ub.edu
[c] Zernike Institute of Advanced Materials, University of Groningen, Netherlands
[d] National Center for Computational Sciences, Oak Ridge National Laboratory, Oak Ridge, TN 37831-6373, U. S. A.
[e] Department of Chemistry and Biochemistry, University of Alabama, Tuscaloosa, AL 35487-0336, U. S. A.
[f] ICREA, Pg. Lluís Companys 23, Barcelona, Spain; E-mail: coen.degraaf@urv.cat
¶ Present address: Institute of Physics, University of Freiburg, Germany

† Electronic Supplementary Information (ESI) available: Detailed information on the methodology to calculate the electronic coupling; Cartesian coordinates of the systems; Tetracene DCD-CAS energies and wave functions; couplings with Gallup-Norbeck weighted DCEC; graphical representations of the active orbitals; NOCI energies for diazadiborinine derivative; Detailed description of the computational information for the magnetic coupling calculations; spin density and Mulliken spin populations; J as function of the selection threshold; DDCI versus NOCI-F timings. See DOI: 10.1039/cXCP00000x/

The coupling of spin moments (from now on referred to as magnetic interactions for simplicity) has also been subject of many theoretical studies and among these the difference dedicated configuration interaction (DDCI)[24,25] has emerged as one of the most precise methods for estimating the magnetic coupling strength.[11] The DDCI method is however computationally costly and it is far from trivial to analyze the outcomes to come up with a conceptual interpretation of the coupling strength, although some very insightful studies have been published on the physics of the magnetic coupling based on DDCI.[26–30]

In this contribution we present an alternative computational scheme for both the calculation of the coupling between electronic states and of the magnetic coupling strength. Our implementation of non-orthogonal configuration interaction (NOCI) takes into account the static and dynamic electronic correlation, as most of the previously mentioned methods. However, NOCI does also include full orbital relaxation from the start by expanding the many-electron wave function as a linear combination of a few key electronic configurations, each expressed in their own set of optimal orbitals. This leads to a compact yet accurate wave function that allows for a straightforward analysis by looking at the coefficients of the electronic configurations in the final wave function. Other multiconfigurational wave function based methods, such as the complete active space self-consistent field (CASSCF) method and the already mentioned DDCI, use one set of orthogonal orbitals and therefore an important part of the wave function expansion are excited configurations that take care of orbital relaxation effects, in addition to others that account for electron correlation (note that the two effects are not strictly separable). Moreover, the weights of the electronic configurations relevant for an accurate treatment (think of charge transfer, local excitations, non-Hund states, etc.) are artificially small in most cases because these configurations are usually not expressed in a set of orbitals that best represents them, one typically uses orbitals optimized for the ground state. This makes their relative energy too high and their contribution to the many-electron wave function too small. A proper estimate of the importance of these key configurations requires the construction of a wave function in which the coefficients of the configurations are modified to include the dynamic correlation and orbital relaxation effects.[11,27,31]

On the contrary, NOCI having these effects included from the start allows for a direct readout of the wave function for analysis. Expressing the key configurations in their own set of orbitals comes of course at a price. The use of different orbital sets for different configurations implies that the molecular orbitals of the Slater determinants in the wave function expansion are no longer orthogonal to each other. This makes the calculation of the energy eigenvalues and eigenvectors more complicated than for the standard multiconfigurational approaches with orthogonal orbitals. However, the increasing computer power and the fact that NOCI is very well suited for parallelization[32] has caused a revival of the computational schemes in which the orthogonality restrictions have been removed.[33–48]

In previous work, we have presented the NOCI for fragments (NOCI-F) method, an extension of NOCI to treat an ensemble of molecules or fragments of a continuous system (e.g., ionic solids or parts of a molecule). Emphasis was on the implementation[32,49], efficiency improvements[50] and some applications, mostly focused on singlet fission.[51–55] Although interesting results were reported in these applications, they lacked one important ingredient which we remedy in this contribution. The NOCI-F calculations reported so far do not include the effect of dynamic correlation, which is of course unavoidable for a more quantitative assessment of the coupling between electronic states and (localized) spin moments.

Ideally one would perform the NOCI using wave functions that have included not only the static (or non-dynamic) electron correlation but also account for the effect of intra-molecular dynamic correlation. There is, however, a problem of practical nature to proceed along this way. For a wave function to include dynamic correlation effects one needs to make very long expansions in terms of electron configurations, which makes the calculation of the coupling in a non-orthogonal setting extremely costly. We have implemented two alternative ways of accounting for the dynamic correlation in the NOCI-F approach. The first is based on shifting the diagonal matrix elements of the NOCI matrix by the correlation energy of the many-electron basis functions (MEBFs) spanning the NOCI space. The second method applies explicitly correlated molecular (or fragment) wave functions to construct the MEBFs and is based on the dynamic correlation dressed complete active space (DCD-CAS) method of Pathak Lang and Neese[56] implemented in Orca.[57]

The remainder of this contribution first describes the main characteristics of the NOCI-F method and then explains in more detail how dynamic correlation is accounted for. After giving some general computational information, we illustrate the effect of including dynamic correlation on the calculation of the electronic coupling between states relevant for singlet fission. We first report the results for tetracene focusing on the relative energies of the states involved and their coupling. Thereafter, the effect on the NOCI wave functions is discussed for a diazadiborinine derivative, recently reported as a possible new member of the family of compounds with singlet fission properties.[58] The results section is closed by presenting the NOCI-F results for the magnetic coupling between two organic radicals and how they are affected by the inclusion of dynamic correlation.

In all these examples, we try not only to merely compare results with and without dynamic correlation but also to illustrate the advantage of working with a very compact many-electron wave function, which allows for an immediate analysis of the property under study.

2 Method

2.1 NOCI-F

The core methodology of the evaluation of the hamiltonian matrix element between non-orthogonal determinants is the General Non-Orthogonal Matrix Element (GNOME) algorithm,[59,60] based on the factorization of the transformed co-factors appearing in the expressions of the one- and two-electron contributions. The

basic expressions formulated by Lowdin[61]

$$\langle\Phi_\alpha|\hat{h}|\Phi_\beta\rangle = \sum_{i,j}\langle\phi_i|\hat{h}|\psi_j\rangle\mathbb{S}(i,j) \tag{1}$$

$$\langle\Phi_\alpha|\hat{g}|\Phi_\beta\rangle = \sum_{i<k}\sum_{j<l}\langle\phi_i\phi_k|\hat{g}|\psi_j\psi_l\rangle\mathbb{S}(ik,jl) \tag{2}$$

with $\mathbb{S}(i,j)$ and $\mathbb{S}(ik,jl)$ the first- and second-order co-factors of the overlap matrix S of the spinorbitals in the two determinants. By applying a corresponding orbital transformation, these expressions can be simplified to

$$\langle\Phi_\alpha|\hat{h}|\Phi_\beta\rangle = \sum_i\langle\tilde{\phi}_i|\hat{h}|\tilde{\psi}_i\rangle\prod_{m\neq i}\lambda_m \tag{3}$$

$$\langle\Phi_\alpha|\hat{g}|\Phi_\beta\rangle = \sum_{i<k}\langle\tilde{\phi}_i\tilde{\phi}_k|\hat{g}|\tilde{\psi}_i\tilde{\psi}_k\rangle\prod_{m\neq i,k}\lambda_m. \tag{4}$$

with $\langle\tilde{\phi}_i|\tilde{\psi}_j\rangle = \lambda_i\delta_{ij}$. After introducing the expansion of the corresponding orbitals $\tilde{\phi}_i$ and $\tilde{\psi}_i$ in a set of basis functions $\{\chi_i\}$ (atomic orbitals or functions from the common molecular orbital basis set[50]), the two-electron contribution turns into

$$\sum_{p<r}\sum_{q<s}\langle\chi_p\chi_r|\hat{g}|\chi_q\chi_s\rangle B(pr,qs) \tag{5}$$

where $B(pr,qs)$ is a transformed second-order co-factor.

$$B(pr,qs) = \frac{1}{2}(1-\hat{P}_{pr})(1-\hat{P}_{qs})\sum_{k,i}\tilde{c}_{ip}\tilde{c}_{kr}\tilde{d}_{qi}\tilde{d}_{sk}\prod_{m\neq i,k}\lambda_m, \tag{6}$$

where $\tilde{c}_i$ and $\tilde{d}_i$ are the expansion coefficients of the corresponding orbitals in the chosen basis set. This transformed co-factor can be factorized as a product of two matrices $F(\omega)$ and $G(\omega)$ of dimension N^2 (N is the number of basis functions), which depend on ω, the number of singularities in the overlap matrix S, that is, the number of λ's that are equal to zero.

$$F(0)_{pq} = \frac{1}{2}\sum_i\tilde{c}_{ip}\tilde{d}_{qi}\lambda_i^{-1} \quad G(0)_{pq} = 2F(0)_{pq}\prod_i\lambda_i \tag{7}$$

$$F(1)_{pq} = \sum_{i\neq m}\tilde{c}_{ip}\tilde{d}_{qi}\lambda_i^{-1} \quad G(1)_{pq} = \tilde{c}_{mp}\tilde{d}_{qm}\prod_{i\neq m}\lambda_i \quad (\lambda_m = 0) \tag{8}$$

$$F(2)_{pq} = \tilde{c}_{np}\tilde{d}_{qn} \quad G(2)_{pq} = \tilde{c}_{mp}\tilde{d}_{qm}\prod_{i\neq m,n}\lambda_i \quad (\lambda_m = \lambda_n = 0) \tag{9}$$

For $\omega = 0,1$, both F and G are zero. The one-electron matrix element is only non-zero for $\omega < 2$ and can be written as

$$\sum_{p,q}\langle\chi_p|\hat{h}|\chi_q\rangle G(\omega) \qquad (\omega = 0,1) \tag{10}$$

These four equations form the basis of the early applications of NOCI to study core-level spectroscopy,[62–64] magnetic coupling[65,66] and electron hopping in transition metal oxides.[67] However, all these studies were based on a NOCI expansion in terms of restricted (open-shell) Hartree-Fock R(O)HF wave functions and only considered a single molecule or (embedded) cluster. To extend the range of application, the NOCI-F method was developed and implemented in GronOR, a massively parallel and GPU-accelerated computer code. NOCI calculations can now be performed on composite systems with more than 100 atoms, applying multiconfigurational wave functions of considerable length for each constituting fragment.

The method starts with the calculation of the relevant electronic states of the fragments a, b, c, etc.

$$\begin{aligned}
\Psi_a^1 &= c_{a,1}\Phi_1 + c_{a,2}\Phi_2 + c_{a,3}\Phi_3 + \ldots \\
\Psi_a^2 &= d_{a,1}\Phi_1' + d_{a,2}\Phi_2' + d_{a,3}\Phi_3' + \ldots \\
&\vdots \\
\Psi_b^1 &= e_{b,1}\Phi_1'' + e_{b,2}\Phi_2'' + e_{b,3}\Phi_3'' + \ldots \\
\Psi_b^2 &= f_{b,1}\Phi_1''' + f_{b,2}\Phi_2''' + f_{b,3}\Phi_3''' + \ldots \\
&\vdots
\end{aligned} \tag{11}$$

These functions can be each expressed in their own set of optimal orbitals and there are no restrictions on their expansion in determinants. Moreover, different active spaces can be used for the different states, the spin moment and even the number of electrons on the fragments can vary from state to state. The fragment wave functions are then combined to form the many-electron basis functions (MEBFs) of the NOCI by forming antisymmetrized spin-adapted products. We take a system consisting of only two fragments as an example, although there is no such limitation in the formalism or the program. We then get

$$\begin{aligned}
\Psi_{MEBF,1}^{ab} &= \hat{A}\Psi_a^1\Psi_b^1 \\
\Psi_{MEBF,2}^{ab} &= \hat{A}\Psi_a^1\Psi_b^2 \\
&\vdots \\
\Psi_{MEBF,N}^{ab} &= \hat{A}\Psi_a^p\Psi_b^q
\end{aligned} \tag{12}$$

Combinations of fragment wave functions must be chosen such that the spin moment and number of electrons of all MEBFs are the same. The spin coupling of the fragment wave functions has been generalized through the use of Clebsch-Gordan coefficients. When more than two fragments are studied the intermediate spin coupling for pairs of fragments must be given as input in addition to the total spin moment of the whole ensemble.

Once the MEBFs are constructed, their hamiltonian and overlap matrices are calculated. This involves a large number of matrix elements between determinants of the MEBFs. For example, when two singlet fragment wave functions of 200 determinants are combined to form a MEBF, it will have a length of 40000 determinants. Hence, the calculation of the energy of this MEBF will require the evaluation of $1.6{\cdot}10^9$ matrix elements. Because these contributions can be calculated independently, this can be done in a massively parallel manner. Furthermore, a screening based on the product of the MEBF expansion coefficients has been shown to be very effective to reduce the number of contributions. Leaving out all determinants pairs with $|c_{bra}\cdot c_{ket}| < 10^{-5}$ leads to reliable energies and electronic couplings and reduces the number of

contributions by several orders of magnitude.[50] Solving the general eigenvalue problem, the NOCI energies and wave functions are obtained. In addition, the electronic coupling between two MEBFs can be determined as

$$\gamma_{ij} = \frac{H_{ij} - \frac{1}{2}(H_{ii} + H_{jj})S_{ij}}{1 - S_{ij}^2} \tag{13}$$

Note that this is equivalent to the hamiltonian matrix element between two mutually Löwdin-orthogonalized MEBFs.

2.2 Dynamic correlation

As mentioned in the introduction, we have used two approaches to introduce dynamic correlation in the NOCI calculation. The first consists basically of shifting diagonal elements of the hamiltonian matrix of MEBFs and is rather straightforward. One first calculates the correlation energy for each fragment wave function, typically by performing a multiconfigurational second-order perturbation theory calculation, but it can be done with any electronic structure method that accounts for dynamic correlation. The most commonly applied methods to estimate the correlation correction are the complete active space and the *n*-electron valence second-order perturbation theory (CASPT2 and NEVPT2). The latter applies the Dyall hamiltonian as zeroth-order hamiltonian[68] and contains, contrary to the Fock-like zeroth-order hamiltonian adopted in CASPT2, two-electron terms for the active orbitals. This leads to an, in principle, more accurate perturbation theory and a complete disappearance of the intruder state problem. However, there is no consensus in the literature which method provides the most accurate relative energies, and there seem to be contradictory opinions about the necessity of applying the ionization potential-electron affinity (IPEA) shift in the CASPT2 method.[69–72] The variations in the results obtained with standard orthogonal approaches discussed in these studies will of course also have their influence on the NOCI-F calculations, an example will be given in the last section of the discussion of the results.

The total shift for each MEBF is taken as the sum of the correlation energies of the fragment wave functions Ψ_i from which the MEBF was constructed. Since not only the orbitals but as a consequence also the determinants and the MEBFs are mutually non-orthogonal, the MEBF basis is first orthogonalized

$$\Psi_j^{\perp} = \sum_i c_{ij}\Psi_i \tag{14}$$

and then the dynamic correlation energy correction is added to the diagonal elements of the hamiltonian matrix in terms of this orthogonalized MEBF basis. Applying the shift to the NOCI matrix expressed in non-orthogonal MEBFs would artificially affect the relative energies of the final NOCI states (see Sec. 1 of the ESI for a more detailed discussion). By default the correction applied to $\Psi_j^{\perp}$ is the shift obtained for the MEBF Ψ_i that has the largest coefficient c_{ij} in Eq. 14, but a weighted average can also be applied,[73] where the weights are calculated using the procedure proposed by Gallup and Norbeck for non-orthogonal configurations.[74]

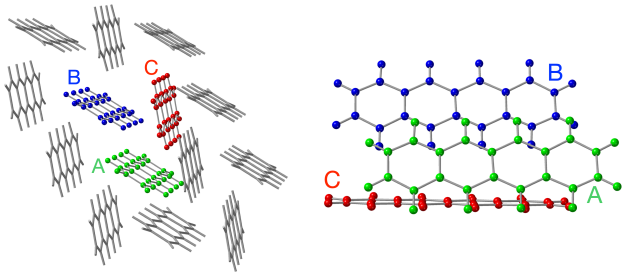

Fig. 1 A (green), B (blue) and C (red) tetracene monomers. Left: view of the three monomers in the crystal along the c-axis. Right: view along the b-axis to illustrate the slight difference of the A-C and B-C interaction.

The second approach involves a second-order dressing of the fragment wave functions with dynamic correlation effects by DCD-CAS. This is done through diagonalizing the effective hamiltonian that in its most elementary form is given by

$$H_{ij} = \langle\Psi_i|\hat{H}|\Psi_j\rangle - \sum_{\kappa}\frac{\langle\Psi_i|\hat{H}^D|\Psi_\kappa\rangle\langle\Psi_\kappa|\hat{H}^D|\Psi_j\rangle}{E_\kappa - E_i}, \tag{15}$$

where $\hat{H}^D$ is the Dyall hamiltonian,[75] Ψ_κ a perturber in the first-order interacting space and E_κ and E_i the expectation values of $\hat{H}^D$. For a more detailed discussion of the DCD-CAS method the reader is referred to Ref. 56. We have used the bias corrected version of the method. These dressed fragment wave functions are then used in the usual way to construct the MEBFs, and from there the NOCI energies and wave functions.

3 Computational information

Computer codes: All NOCI-F calculations were performed with GronOR,[32] while all the calculations on the fragments were done with OpenMolcas,[76] except for the DCD-CAS calculations for which we have used the Orca code.[57]

Structures: Geometries for the tetracene calculations were taken from the experimental crystal structure.[77] Three different dimers can be defined which we labelled AB, AC and BC, respectively as shown in Fig. 1. Fragment A and B are identical and connected by the inversion symmetry of the $P\bar{1}$ space group. The AB cluster is used to calculate the coupling within a stack. Dimers AC and BC give information about the inter-stack coupling.

The general structure of diazadiborinine is depicted in the left panel of Fig. 2. The derivative that we have studied here has R_1 = R_2 = H, and R_3 = CH_3. Because no experimental crystal structure is available for this derivative, we have optimized the lattice positions and the unit cell parameters starting with the crystal structure of the derivative with R_1 = R_2 = H, and R_3 = phenyl.[78] The space group $C2/c$ of the parent compound is kept. The geometry optimization is done with Crystal-17[79] and a detailed overview of the computational settings can be found in Sec. 3 of the ESI. The relative orientation of the molecules in the unit cell, shown in the right panel of Fig. 2 remains basically unchanged compared to the initial structure. The only obvious difference is a shortening of the unit cell in the c-direction from 18.9 Å in the initial structure to 11.8 Å in the structure with methyl groups. This is in

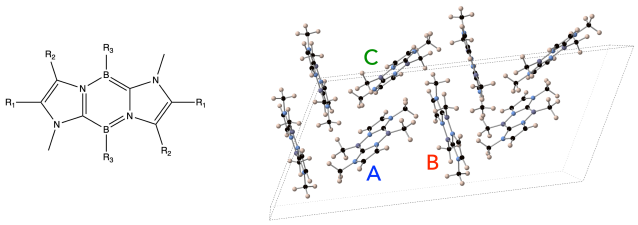

Fig. 2 Structure of the diazadiborinine molecule (left) and the optimized crystal structure (right) of the variant with R_1=R_2=H; R_3=CH_3. The molecules labeled with A, B and C are used to form the dimers.

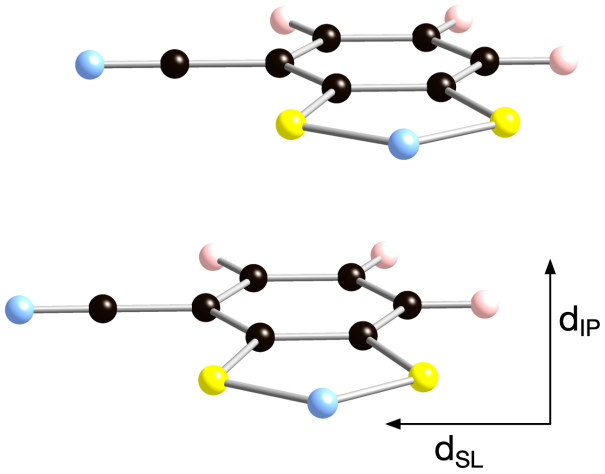

Fig. 3 4-NCBTA dimer. Black spheres represent C, blue is N, yellow is S and pink is H. Five conformations are studied: geometry 1 (d_{SL}= 2.25 Å, d_{IP}= 2.50 Å), geometry 2 (d_{SL}= 1.50 Å, d_{IP}= 3.80 Å), geometry 3 (d_{SL}= 1.25 Å, d_{IP}= 3.50 Å), HT(300K) (d_{SL}= 1.01 Å, d_{IP}= 3.52 Å) and LT(180K) (d_{SL}= 0.00 Å, d_{IP}= 3.286 Å) .

line with the orientation of the larger phenyl groups in the experimental structure, basically along the c-direction.

The calculations on the organic radicals pyrazinedothiazolyl (PDTA) and 4-cyanobenzo-1,3,2-dithiazolyl (4-NCBDTA) are done with the DFT (B3LYP/6-31+G(d)) optimized fragments taken from Ref. 80. Five different conformations were studied for 4-NCBDTA: an eclipsed pair, representative of the low-temperature (LT) crystal structure,[81] a slipped pair placed at the geometry corresponding to the crystal of the high-temperature (HT) polymorph[81] and three additional conformations varying the slippage and interplanar distances (d_{SL} and d_{IP}), see Figure 3) as defined by Francese *et al.*, who studied magnetic interactions in 4-NCBDTA dimers using DFT.[80] For PDTA, we have performed a series of calculation in with d_{IP} was kept constant at 3.0 Å and d_{SL} was varied from 1.0 Å to 3.25 Å.

One-electron basis sets: The fragment calculations with OpenMolcas were all done with basis sets from the internal ANO-RCC library containing basis sets optimized for scalar relativistic effects and core-correlation.[82] The following contractions were used: (3s,1p) for H; (4s,3p,1d) for B, C, N: and (5s,4p,1d) for S. In the case of the DCD-CAS calculations performed with Orca, we have opted for the def2-TZVP basis set to expand the orbitals.

Active space: In all fragment calculations, we have used active spaces that cover the most relevant part of the π-space. The details of each space is given in the discussion of the results as they change from case to case. Graphical representations of the active orbitals are included in the ESI (Fig. S2). The CASPT2 calculations were done with a level shift of 0.15 au., using the standard IPEA=0.25 zeroth-order hamiltonian, except stated otherwise. All electrons except the deep core ones (B,C,N-1s^2; S-1s^2,2s^2,2p^6) were correlated.

4 Results

To put the results described in the next two section in a framework, we first give a very short description of the singlet fission phenomena. Singlet fission can occur in materials with chromophores that have their first triplet state approximately halfway the excitation energy of the first excited singlet: $E(S_1) \gtrsim 2E(T_1)$. When such a chromophore absorbs a photon that brings it to the S_1 state, part of the energy can be transferred to a neighbouring molecule inducing there the population of the T_1 state, while the chromophore itself also falls back in the T_1 state. The resulting singlet state built from the two coupled triplets (^1TT) has two electron-hole pairs, which might separately diffuse. When implemented in solar cells based on organic materials, this process has the potential to increase the efficiency of such devices. In addition to the energy condition, the occurrence of singlet fission also needs a sufficiently large electronic coupling between the excited singlet state S_1S_0 and the final state ^1TT. This coupling can either be calculated as a direct coupling only involving the diabatic representation of the initial $S_1S_0 \pm S_0S_1$ and ^1TT states or by extending the description with a charge transfer enhanced mechanism in which the two states have incorporated the effect of charge transfer excitations between the two involved chromophores (see Sec. 2 of the ESI for a more detailed description of how this CT enhanced coupling is calculated).

Sec. 4.1 discusses the influence of dynamic electron correlation on the direct and charge-transfer enhanced coupling in tetracene, a prototype singlet chromophore and Sec. 4.2 is centered on the analysis of the NOCI wave function and how it changes when dynamic correlation is accounted for. The treatment of dynamic electron correlation in NOCI-F can of course also be used for applications other than singlet fission. In Sec. 4.3 we switch topics and discuss the magnetic coupling in organic radicals.

To distinguish the results before and after considering the dynamic electron correlation, we label the outcomes of the calculations with "*no DCEC*" and "*DCEC*", respectively (DCEC stands for dynamic correlation energy correction).

4.1 Tetracene: electronic coupling

Table 1 lists the relative energies of the different states of the three tetracene molecules considered, A, B and C (see Fig. 1). D^+ and D^- denote the doublet states that arise from ionization and electron addition, respectively. The latter states are used to construct the charge transfer MEBFs (D^+D^- and D^-D^+) for the NOCI. The CASPT2 energies obtained with a CASSCF(8,8) reference wave function are close to those calculated with the larger active space in all cases.

We use the CASSCF(8,8) monomer wave functions for the con-

Table 1 Relative energies (in eV) for the three tetracene molecules

	CASSCF(8,8)	CASPT2	CASSCF(14,14)	CASPT2
fragments A and B				
S_0	0.00	0.00	0.00	0.00
S_1	3.87	3.01	3.88	3.16
T_1	1.87	1.45	1.62	1.50
D^+	6.03	6.75	6.08	6.72
D^-	0.55	-0.58	0.81	-0.57
fragment C				
S_0	0.00	0.00	0.00	0.00
S_1	4.00	3.07	4.28	3.22
T_1	2.08	1.66	1.52	1.85
D^+	6.12	6.80	5.82	6.99
D^-	0.75	-0.49	0.65	-0.35

Table 2 Direct and total electronic coupling (in meV) between ^1TT and S_0S_1/S_1S_0 combinations for the AB, AC and BC tetracene dimers based on CASSCF(8,8) fragment wave functions. The DCEC couplings are obtained after shifting the diagonal matrix elements with the correlation correction.

dimer	no DCEC		DCEC	
	direct	total	direct	total
AB	0.0	0.1	0.0	0.1
AC	0.4	1.3	0.4	8.4
BC	1.1	2.3	1.1	21.6

struction of the six MEBFs and apply a threshold of $|c_{bra} * c_{ket}| > 10^{-5}$ to include determinant pairs of *bra* and *ket* MEBFs in the calculation of the 6×6 NOCI hamiltonian and overlap matrices. This reduces the total number of contributions from $1.8 \cdot 10^{13}$ to $4.7 \cdot 10^8$ for the calculation of the 21 unique $\hat{H}$ and $\hat{S}$ matrix elements.

Fragment A and B belong to the same stack and lie parallel to each other. This results in an almost complete delocalization of the local singlet excited state over the two fragments, but also to a negligible coupling with the ^1TT state. Table 2 show that neither the direct nor the total coupling (i.e. the direct coupling plus the CT enhanced coupling) reach values that are significant. Applying the dynamic correlation shift on the diagonal does not change the coupling, it remains close to zero. The situation is quite different for the inter-stack coupling. Both AC and BC show couplings between the ^1TT and $S_0S_1 - S_1S_0$ states that are significantly larger. Contrary to the AB dimer, the excited singlet state remains almost completely localized on one of the fragments, and hence, in- and out-of-phase combinations of S_0S_1 and S_1S_0 loose there meaning somewhat. First, we observe that the direct coupling is quite small in both cases, and that dynamic correlation does not change these values. When dressing the diabatic states with charge transfer configurations, the total coupling becomes much larger and we also observe a sizeable effect of applying the correlation energy shift. This is directly related to the energy lowering of the CT MEBFs when dynamic correlation is included, as shown in Table 3.

The couplings with DCEC reported in Table 2 are obtained applying the shift corresponding to the dominant MEBFs in the orthogonalized basis. The comparison with the alternative approach of applying a shift determined by the weighted averaged of MEBFs is given in the ESI (Tables S3 and S4), but gives results that are less than 0.1 meV different from those listed in the Table.

Table 3 MEBF energies (in eV, relative to the S_0S_0 MEBF) of the three tetracene dimers before and after applying a shift for the dynamic electron correlation.

dimer	S_0S_1	S_1S_0	^1TT	D^+D^-	D^-D^+
no DCEC					
AB	3.81	3.83	3.15	4.98	4.99
AC	4.22	3.88	3.51	5.20	4.71
BC	4.22	3.89	3.50	5.17	4.68
DCEC					
AB	3.51	3.51	3.22	3.95	3.94
AC	3.82	3.48	3.57	4.16	3.68
BC	3.64	3.49	3.44	4.14	3.64

Before accounting for the dynamic correlation by applying the shift there is a clear gap between the MEBFs that describe the local excited singlet states and the CT: about 1 eV for the AB dimer and somewhat smaller for the AC and BC. This gap becomes much smaller (AB) or even non-existent (AC,BC) when dynamic correlation is taken into account. This causes a much larger mixing between S_0S_1, S_1S_0 and ^1TT MEBFS on the one side and D^+D^- and D^-D^+ on the other, and therefore, to significantly increased coupling, especially for the AC and BC dimers, as reflected in Table 2.

In addition to the shift in the energy, dynamic correlation could in principle also affect the monomer wave functions used to construct the MEBFs of the NOCI calculation. Following the above-described strategy based on the DCD-CAS approach we compare here the couplings in the three tetracene dimers obtained with CAS(6,6) wave functions to those obtained with wave functions modified by the effect of dynamic correlation. The reason for the reduction of the active space to 6 electrons and 6 orbitals is the fact that the DCD-CAS with the larger active space is computationally very expensive. The monomer energies of the CASSCF(6,6) and subsequent DCD-CAS are not substantially different from the ones listed in Table 1 and can be found in Table S6 of the ESI.

Table 4 compares the CASSCF(6,6) and DCD-CAS wave function expansions in terms of electronic configurations for the ground state of fragment A, the green molecule in Fig. 1. It shows that absorbing the effect of dynamic correlation in the coefficients of the configurations belonging to the CAS tends to increase the weight of the leading configuration. The same tendency is observed for all the other electronic states in all three fragments (see Table S5 of the ESI).

Table 5 shows that the direct coupling between the S_0S_1 and ^1TT MEBFs is hardly affected by the inclusion of dynamic correlation in the wave function; for all three dimers the coupling is practically the same when calculated with CASSCF(6,6) or DCD-CAS fragment wave functions. However, this coupling in tetracene is basically too small to be conclusive about the effect of using explicitly correlated wave functions.

The picture changes substantially when we look at the total couplings after adding the effect of the CT states (Table 6). At first

Table 4 Weights of the six most important electronic configurations in the CASSCF(6,6) and DCD-CAS(2) wave function of the ground state of tetracene molecule A. The electronic configuration is given by the occupation number of the six active orbitals.

El. configuration	CASSCF(6,6)	DCD-CAS
2 2 2 0 0 0	0.872	0.929
2 2 0 2 0 0	0.042	0.026
2 1 1 1 1 0	0.032	0.017
2 0 2 2 0 0	0.014	0.007
1 1 2 0 1 1	0.011	0.005
0 2 2 0 0 2	0.007	0.003
Total	0.983	0.989

Table 5 Direct electronic couplings (in meV) between S_0S_1 and ^1TT for three tetracene dimers based on CAS(6,6) and DCD-CAS fragment wave functions.

dimer	CASSCF	DCD-CAS
AB	0.0	0.0
AC	1.5	1.7
BC	0.6	0.7

sight, important changes in the coupling are introduced when the CASSCF(6,6) wave function is replaced by a DCD-CAS wave function. However, it should be taken into account that the relative energies of the correlated fragment wave functions are quite different for both methods (see ESI, Table S2), and this distorts the comparison. The results for tetracene described above confirm results from earlier studies that when the effect of the CT states is included, the coupling is substantially influenced by the relative energies of the states involved in the process. When the CT states are closer to the ^1TT and $S_1S_0 \pm S_0S_1$ states, the coupling increases accordingly. Since we are trying to establish to what extent changes in the wave function caused by dynamic correlation rather than the changes in energy affect the couplings, the comparisons are also done by applying a shift on the diagonal elements of the NOCI matrix so that they match in both cases the CASPT2 energies calculated before.

This adjustment in the energies brings the total couplings based on a DCD-CAS wave function back in agreement with those calculated with CASSCF(6,6) wave functions, showing that the changes in the wave function due to dynamic correlation (listed in Table 4) are not large enough to qualitatively change the electronic couplings between the MEBFs. The values of the couplings based on the CASSCF(6,6) fragment wave functions are slightly larger than those listed in Table 2 calculated with the CASSCF(8,8) functions, but show the same trend.

Table 6 Total electronic couplings (in meV), direct plus CT enhanced, between S_0S_1 and ^1TT for three tetracene dimers based on CAS(6,6) and DCD-CAS fragment wave functions, before and after applying a shift on the diagonal of the NOCI matrix.

	no DCEC		DCEC	
dimer	CASSCF	DCD-CAS	CASSCF	DCD-CAS
AB	0.2	0.1	0.3	0.2
AC	10.7	5.6	12.8	14.0
BC	14.5	3.3	39.8	35.2

As a second check on the importance of including dynamic correlation effects in the wave functions used in NOCI, we performed calculations on a hypothetical benzene dimer. Here, we calculated the direct coupling as function of the distance between the two benzene molecules though NOCI-F with the same type of MEBFs as in the previously described tetracene dimers. The two molecules lie parallel in the $x-y$ plane and are displaced with respect to each other along x and y by 1.25 Å and 2.25 Å respectively. In this geometry, the direct coupling is large enough to study the influence of dynamic correlation on the wave function. Starting at 3.75 Å the distance between the dimers was reduced to 3.00 Å in three steps and the direct coupling between the S_0S_1 and ^1TT MEBFs was calculated with CASSCF(6,6) and DCD-CAS wave functions. The couplings are very similar at all four distances, ranging from 2.07 and 2.31 meV for CASSCF(6,6) and DCD-CAS at 3.75 Å to 15.14 and 15.97 meV at 3.00 Å. Since the relative energies of the S_1S_0 and ^1TT states that are involved in this direct coupling are almost unaffected, these values hardly change when the MEBF energies are shifted to their CASPT2 value, see ESI, Table S7.

As these results show that incorporating the dynamic electron correlation into the wave function does not significantly affect the electronic couplings (and is computationally quite demanding), we only apply the shifting approach in the next two sections.

4.2 Diazadiborinine: NOCI wave function

One of the convenient points of the NOCI-F approach is the fact that the final wave function is (i) extremely short and (ii) expressed in terms of many-electron basis functions with a clear character. This makes the interpretation of the wave function a relatively easy task. Here, we present the NOCI wave functions of three pairs of diazadiborinine molecules as they were found in the optimized crystal structure (see Fig. 2). Diazadiborinines have recently been presented as possible singlet fission chromophores based on calculations of isolated molecules with different substituents.

Similar to the tetracene case, two diazadiborinine molecules (A and C) have an almost parallel orientation, while the molecular plane of B is nearly perpendicular to these two units. Without taking into account the effect of dynamic electronic correlation, the NOCI states dominated by the S_0S_1/S_1S_0 MEBFs lie approximately 3.7 eV above the ground state in the three dimers, the electronic state with the largest ^1TT contribution is found around 2.5 eV. The relative energy of the charge transfer states ranges from 4.4 eV for BC to 5.5 eV for AC. Dynamic correlation lowers the energy of the NOCI states with large S_0S_1/S_1S_0 character giving rise to three almost degenerate electronic states in all three clusters. The charge transfer states are also lowered in energy and for the BC cluster they become almost degenerate with the other three low-lying excited states (see ESI, Table S10). The direct coupling of the S_0S_1/S_1S_0 MEBFs with ^1TT is 5.0 meV for AB and practically zero for the other two dimers. The couplings obtained after adding the effect of the CT states show a similar tendency: almost no coupling for the parallel molecules A and C,

Table 7 MEBF coefficients of six NOCI wave functions for three diazadiborinine dimers

MEBF	Ψ_1	Ψ_2	Ψ_3	Ψ_4	Ψ_5	Ψ_6
AB dimer						
S_0S_0	**0.998**	-0.014	0.0029	0.020	0.007	0.084
S_0S_1	0.005	-0.001	**0.698**	**0.709**	0.111	0.014
S_1S_0	0.027	-0.004	**0.697**	**-0.705**	0.127	-0.035
^1TT	0.004	**0.992**	0.005	-0.007	0.004	0.133
D^+D^-	-0.023	-0.061	0.106	-0.024	**-0.683**	**0.721**
D^-D^+	-0.023	-0.061	-0.093	-0.009	**0.718**	**0.689**
AC dimer						
S_0S_0	**1.000**	0.000	0.029	0.019	0.004	0.007
S_0S_1	-0.013	0.000	-0.032	**0.999**	0.005	-0.001
S_1S_0	0.006	0.000	**1.000**	0.032	0.001	-0.015
^1TT	0.000	**1.000**	0.000	0.000	0.004	0.002
D^+D^-	-0.010	0.000	0.008	0.001	0.000	**1.000**
D^-D^+	0.000	-0.001	-0.001	-0.003	**1.000**	0.000
BC dimer						
S_0S_0	**1.000**	-0.002	0.019	0.029	0.024	0.017
S_0S_1	-0.018	0.000	**-0.314**	**0.948**	0.044	-0.020
S_1S_0	0.010	0.000	**0.948**	**0.317**	-0.035	0.044
^1TT	0.001	**0.999**	0.000	-0.001	0.037	0.033
D^+D^-	-0.009	-0.020	-0.037	0.006	-0.006	**0.999**
D^-D^+	-0.012	-0.031	0.043	-0.027	**0.998**	0.007
BC dimer with DCEC						
S_0S_0	**1.000**	0.020	0.028	-0.011	0.025	0.020
S_0S_1	-0.018	**-0.279**	**0.953**	-0.075	0.086	-0.038
S_1S_0	0.010	**0.953**	**0.287**	-0.014	-0.066	0.082
^1TT	0.000	-0.001	0.062	**0.964**	**0.219**	**0.137**
D^+D^-	-0.012	-0.083	0.008	**-0.116**	-0.055	**0.988**
D^-D^+	-0.014	0.081	-0.074	**-0.213**	**0.970**	0.037

weak coupling (2.1 meV) for B and C due to their larger separation, and a moderate coupling of 8.0 meV for the AB dimer. A more detailed overview of the NOCI energies can be found in the ESI (Table S11), but here we focus on the analysis of the NOCI wave function to interpret the nature of the excited states.

In this analysis, we will follow the nomenclature of Bäppler and co-workers[83] (recently used by some of us)[55], which distinguishes different excitonic and charge transfer states. That analysis is based on the descriptors that can be extracted from the interpretation of the 1-electron transition density matrix[84], but here we base the analysis on a direct read-out of the wave function. Starting with the AB dimer, Table 7 shows that Ψ_3 and Ψ_4 are equal mixtures of the S^0S^1 and S^1S^0 MEBFs, which qualifies these excited states as so-called excitonic resonance (ER) states. The MEBF coefficients of Ψ_5 and Ψ_6 are small for the first four MEBFs, and also show a fifty-fifty contribution of the D^+D^- and D^-D^+ MEBFs, indicative of so-called charge resonance (CR) states. The first two functions can be considered as pure S_0S_0 and ^1TT states. The excited states of the AC dimer has quite a different character. Instead of ER and CR states, the NOCI wave functions show that the AC geometry leads to localized excitonic (LE) and local charge transfer (CT) states. The two lower states have again only contributions from one MEBF. Finally, the singlet excited states of the BC dimer are mostly LE states, but show a non-negligible delocalization contribution making these states mixed LE/ER states. The higher lying excited states (Ψ_5 and Ψ_6) are pure CT states. Finally, we compare the wave functions of the BC dimer before and after applying the dynamic correlation correction. The S_0S_1/S_1S_0 dominated wave functions become slightly lower in energy than the ^1TT dominated function but do not significantly change their character when dynamic correlation is accounted for. On the other hand, the CT states stay localized but pick up some ^1TT character, which is also reflected in Ψ_4, which in addition to the large contribution from the ^1TT MEBF, also has sizeable coefficients on the CT MEBFs.

4.3 Magnetic coupling

Another field of application of the NOCI-F method is the study of the magnetic coupling between spin moments in molecular compounds. The spin-coupling strength between two fragments A and B (molecules, metal magnetic centers or parts of a molecule), J_{AB}, is evaluated from the isotropic Heisenberg hamiltonian

$$\hat{H}_H = -J_{AB}\hat{S}_A \cdot \hat{S}_B \tag{16}$$

in terms of energy differences between the spin states resulting from the different couplings of the local spin moments. Depending on the system, the magnetic coupling can be of very small magnitude and thus difficult to compute accurately. Therefore, it is important to assess to what extent dynamic correlation affects the energy differences between the electronic spin states obtained.

First, the magnetic interaction between a pair of 4-cyanobenzo-1,3,2-dithiazolyl (4-NCBDTA) radicals is studied. For this system, the local spins of the radicals, S_A and S_B, are 1/2 and therefore the magnetic coupling, J_{AB}, can be estimated as the energy difference between the singlet and triplet states of the pairs. A negative J-value is indicative for an antiferromagnetic coupling (singlet below triplet). Here, we compute the coupling between two radicals belonging to the same stack. It has been previously shown that the interactions between radicals located at different stacks (inter-stack) are much smaller than those within a stack.[85]

To describe the 4-NCBDTA monomers we perform CASSCF calculations with two different active spaces, a CAS(3,3) including 3 π orbitals and 3 electrons and a CAS(5,5), with 5 electrons in 5 orbitals. The unpaired electron is mainly located on the N atom of the S-N-S moiety, as illustrated in section 4.2 of the ESI. For each radical, five electronic states have been considered: the doublet ground state, D_0, the first excited doublet state, D_1, two anionic/cationic singlet states in which the monomer wins or looses one electron, S^- and S^+, respectively, and an acceptor triplet state, T^-. The T^+ state lies much higher in energy (>9 eV above D_0), because it involves ionisation from the highest doubly occupied orbital instead of the singly occupied molecular orbital as in the S^+ state. For this reason, T^+ has not been considered in the NOCI-F.

Results in Table 8 show that the relative energies between the different states with respect to the doublet ground state, D_0, do not vary significantly with the size of the active space. Inclusion of dynamic electron correlation by CASPT2 decreases the excitation energies and leads to nearly the same values irrespective of

the CAS applied. CASPT2 calculations have been performed using the standard zeroth-order hamiltonian (with an IPEA shift of 0.25 a.u.) and without IPEA shift (CASPT2-0). For the monomer, the inclusion of the IPEA shift in the diagonal Fock matrix elements of the active orbitals has only a small effect on the relative energies, however the impact of this shift could be more significant for the magnetic coupling of two monomers. It has been suggested in previous studies that CASPT2(0), with the original choice of the zeroth-order hamiltonian, leads not only to couplings closer to experiment, but also reproduces more accurately the expected spacing between spin states when treating systems with $S>\frac{1}{2}$.[86] CASPT2(0) on top of a CASSCF(5,5) places the acceptor singlet and triplet states around 0.7 eV below the D_0 state, the excited doublet D_1 lies 2.5 eV above the D_0 state, and the donor state S^+ is 7.0 eV higher than D_0.

From the CASSCF(3,3) and CASSCF(5,5) wave functions of the monomers, the MEBFs for the singlet and triplet states of the different dimers are constructed. Since the magnetic coupling is usually a small quantity, it can be sensitive to the threshold applied on the product of the CI coefficients to be considered to construct the NOCI hamiltonian and overlap matrices. For this reason, we have explored the variation of the J_{AB} value obtained by the NOCI-F approach with the threshold on the determinant pair coefficients included in the non-orthogonal CI. Results show that a more severe limit is needed than the usual 10^{-5} value applied to the study of electron excitations (see Fig. S4 of the ESI). Here, the singlet-triplet energy difference is only fully converged with a threshold of 10^{-7} when the MEBFs are constructed from the CASSCF(3,3) wave functions and 10^{-8} when they are built from monomer CASSCF(5,5) wave functions. The total number of determinant pairs is much larger when the MEBFs are based on a monomer CASSCF(5,5) wave function and, hence, the contributions to the hamiltonian matrix elements are scattered in a longer list.

To evaluate the different contributions to the magnetic coupling, the energy of the singlet and triplet states have been computed by NOCI calculations of different size (see Table 9). First, a direct singlet and triplet coupling within the ground state D_0D_0 MEBF is considered (GS in Table 9). Addition of the excited doublet states, D_0D_1, D_1D_0 and D_1D_1, leads to 4x4 non-orthogonal hamiltonian spin singlet and triplet matrices and permits to evaluate the influence of the local excited states on the value of J_{AB} (GS + excited doublets). The role of charge transfer states between radicals can be studied by including the S^-S^+ and S^+S^- MEBFs giving a 3×3 hamiltonian matrix for the singlet state and likewise T^-S^+ and S^+T^- for the final triplet state (GS + CT). Finally, a 6×6 NOCI calculation including all six possible MEBFs (D_0D_0, D_0D_1, D_1D_0, D_1D_1, S^-S^+, S^+S^- for the singlet state and D_0D_0, D_0D_1, D_1D_0, D_1D_1, T^-S^+, S^+T^- for the triplet) is performed allowing for both excitation and charge transfer effects (GS + CT+ excited doublets). Results in Table 9 show that for all the geometrical conformations, inclusion of the excited doublet states in the CI has an insignificant effect, whereas the incorporation of charge transfer states turns out to be essential and greatly affects the J_{AB} value. Notice that the inclusion of charge transfer configurations stabilizes the singlet state when the magnetic coupling is antiferromagnetic (geometries 2 and 3, HT and LT) while it favours the triplet state for the ferromagnetic coupling (geometry 1). This effect is not caused by changes in the relative energies of the singlet and triplet CT states in the different geometries, as the variations among the conformations are practically the same. However, large changes in the couplings between D_0D_0 and the CT states are observed. For example, the triplet CTs have a coupling a approximately 276 meV with the D_0D_0 in geometry 1, which decreases to 35 meV in the HT phase. The opposite trend is observed for the singlet state, where the CT-D_0D_0 coupling increase from 135 meV in geometry 1 to 276 meV in HT.

For two conformations, namely those corresponding to the experimental HT and LT crystal structures, NOCI calculations were also performed constructing the many-electron basis functions as antisymmetrized products of the CASSCF(5,5) monomer wave functions. Results of the magnetic coupling show no substantial difference compared to the values obtained with a CASSCF(3,3).

On the other side, the effect of the remaining dynamic electron correlation on the value of the magnetic coupling has been considered by applying the shifting strategy explained in the Method section. The results reported in Table 9 show an important increase of the absolute values of J_{AB} when including the correlation correction, and evidences that the correlation correction using the standard IPEA shift, CASPT2(0.25), leads to a larger stabilization of the singlet state compared to CASPT2(0). In any case, all conformations, except for the one corresponding to geometry 1, show an antiferromagnetic coupling, being largest for the LT structure where the two monomers are one on top of each other in an eclipsed position.

To asses the reliability of the magnetic coupling values calculated by the NOCI-F technique, we have also carried out calculations with other standard computational approaches that have been extensively used in the literature.[11] Three different methodologies have been applied to compute J_{AB} on the five dimers studied. First, Density Functional Theory calculations using the unrestricted B3LYP exchange-correlation hybrid functional. In second place, supramolecular CASSCF calculations considering two active spaces, a CASSCF(6,6) with 6 π orbitals and 6 electrons, and a CASSCF(10,10) containing 10 π orbitals and 10 electrons, have been performed. To include the effect of the remaining dynamical electron correlation CASPT2 (with and without IPEA shift) and NEVPT2[68,87] calculations have been carried out. Finally, we apply the Difference Dedicated CI approach (DDCI)[24,25] on top of a CAS(2,2) active space formed by the two magnetic orbitals with the two unpaired electrons. In this approach, only the configurations that play a role in the energy difference of the states involved in the magnetic coupling are included in the CI expansion. The DDCI method is considered a benchmark in the field of computational molecular magnetism.[11] The full set of results of the magnetic coupling obtained by the different methods is given in Table S14 of the ESI, where additionally, the computational information of each method is detailed. Table 10 summarizes the most salient results. First, it is worth mentioning that CASSCF calculations lead to almost the same values of J_{AB} for both active spaces, CASSCF(6,6) and CASSCF(10,10). Inclusion of electron correlation by second-order perturbation theory increases the abso-

Table 8 Relative energies (in eV) of the 4-NCBTA radical used in the NOCI-F calculations. CASPT2(0.25) refers to the standard zeroth-order hamiltonian with an IPEA shift of 0.25 a.u. and CASPT2(0) has no IPEA shift (see text).

	CASSCF(3,3)	CASPT2(0.25)	CASPT2(0)	CASSCF(5,5)	CASPT2(0.25)	CASPT2(0)
D_0	0.00	0.00	0.00	0.00	0.00	0.00
D_1	3.20	2.39	2.17	3.24	2.73	2.46
S^-	-0.25	-0.97	-0.73	-0.26	-0.98	-0.73
S^+	6.91	6.78	7.02	6.92	6.74	7.01
T^-	0.92	-0.50	-0.69	0.99	-0.38	-0.62

Table 9 Magnetic couplings, J_{AB}, (in cm^{-1}) between selected 4-NCBTA radical pairs computed by NOCI. MEBFs are constructed from monomer CASSCF(3,3) wave functions. For the HT and LT structures results obtained from CASSCF(5,5) wave functions are shown in parenthesis.

	geometry 1	geometry 2	geometry 3	HT(300 K)	LT(180 K)
GS	37	5	-14	-65 (-65)	-698 (-691)
GS + excited doublets	39	3	-19	-70 (-67)	-700 (-692)
GS + CT	138	-9	-91	-246 (-245)	-2126 (-2117)
GS + CT + excited doublets	139	-13	-101	-258 (-261)	-2151 (2125)
DCEC					
GS + CT + exc. doublets + CASPT2(0.25)	240	-22	-144	-353 (-362)	-2780 (-2789)
GS + CT + exc. doublets + CASPT2(0)	250	-14	-113	-290 (-295)	-2388 (-2366)

lute value of the magnetic coupling, CASPT2(0) and NEVPT2 approaches giving similar values. The CASPT2(0.25) results in the ESI however, reveal a much larger antiferromagnetic contribution, in line with previous studies. Comparing these results with those obtained by DDCI, it can be seen that B3LYP, CASPT2(0) and NEVPT2 tend to overestimate the J_{AB} value. Instead, applying the NOCI-F approach shifting the diagonal elements of the NOCI matrix by the CASPT2(0) electron correlation energy correction, lead to results in good agreement with the values obtained by the DDCI method. Hence, these results validate the NOCI-F approach as a reliable alternative to the DDCI method in the computation of magnetic interactions providing, in addition, a tool to easily interpret the contributions of the different terms to the final value.

To close this section on the application of NOCI-F to the magnetic interaction among organic radicals, we present a comparison of some standard electronic structure methods for a second pair of biradicals, pyrazinedothiazolyl (PDTA), also studied before by Francese *et al.* [80] In this case we fix the interplanar distance d_{IP} to 2.5 Å and gradually increase the lateral slippage from d_{SL} = 1.0 Å to 3.25 Å. The DFT calculations reported in Ref. 80 indicate that the coupling at this interplanar distance ranges from strongly antiferromagnetic to moderately ferromagnetic as function of the slippage. The NOCI-F results are obtained from a 6x6 NOCI with the same MEBFs as for the previously described 4-NCBTA radical pair.

The left panel of Fig. 4 shows that all six methods (B3LYP, CASPT2(0), CASPT2(0.25), NEVPT2, DDCI and NOCI-F) reproduce the same tendency, large antiferromagnetic interactions for small and large slippage values and ferromagnetic coupling at the intermediate d_{SL} values. However, zooming in on the ferromagnetic region (right panel of Fig. 4) interesting differences show up. Again taking the DDCI curve as reference, we see that B3LYP significantly underestimates the ferromagnetic interaction while CASPT2(0.25) predicts far too strong interactions. Furthermore, it is clear that the NOCI-F (with CASPT2(0) shifts) reproduces the DDCI curve in the whole ferromagnetic region with remarkable precision. NEVPT2 and CASPT2(0) also do a decent job but miss some of the details of the DDCI curve. The left panel shows that NOCI slightly overestimates the antiferromagnetic interaction for larger d_{SL} values but stays closer to the DDCI benchmark results than the other approaches. Figure S8 of the ESI shows that NOCI-F without dynamic correlation corrections is not as accurate as the results shown in Fig. 4, fully in line with the observations made for 4-NCBTA.

5 Summary and Conclusions

Dynamic electron correlation is known to have an important effect on the relative energies of different electronic states. Estimates based on multi-configurational wave functions that only incorporate static correlation, such as CASSCF wave functions, do typically not compare favorably with experimental data. More reliable relative energies can be obtained by accounting for the dynamic correlation effects through multi-configurational second-order perturbation implementations such as CASPT2 and NEVPT2. Whereas the effect on the relative energies is large and well-documented, the question to what extent the coefficients of the leading configurations of the wave function suffer changes under the effect of dynamic correlation is less well resolved. For geometries near avoided crossings, dynamic correlation can cause important changes and the magnetic coupling parameter is also importantly affected by changes in the leading configurations in some cases, but generally speaking, dealing with static correlation provides reliable wave functions.

Incorporating the effect of dynamic correlation on the relative energies of the MEBFs is straightforward and has been achieved by shifting the diagonal elements of the NOCI matrix expressed in orthogonalized MEBFs. This procedure neglects the effect of dynamic correlation between electrons on different fragments, which can safely be assumed to be negligible given the short-

Table 10 Magnetic couplings, J_{AB}, (in cm^{-1}) between selected 4-NCBTA radical pairs calculated by various computational approaches.

	geometry 1	geometry 2	geometry 3	HT(300 K)	LT(180 K)
DFT/B3LYP	193	-92	-360	-655	-3476
CASSCF(10,10)	70	3	-38	-153	-1760
CASSCF(10,10)+CASPT2(0)	1122	-82	-270	-564	-3766
CASSCF(10,10)+NEVPT2	1106	-45	-248	-520	-4004
DDCI on CAS(2,2)	289	-30	-153	-317	-2298
NOCI-F CAS(3+3,3+3) + DCEC GS + CT + excited doublets + CASPT2(0)	250	-14	-113	-290	-2388

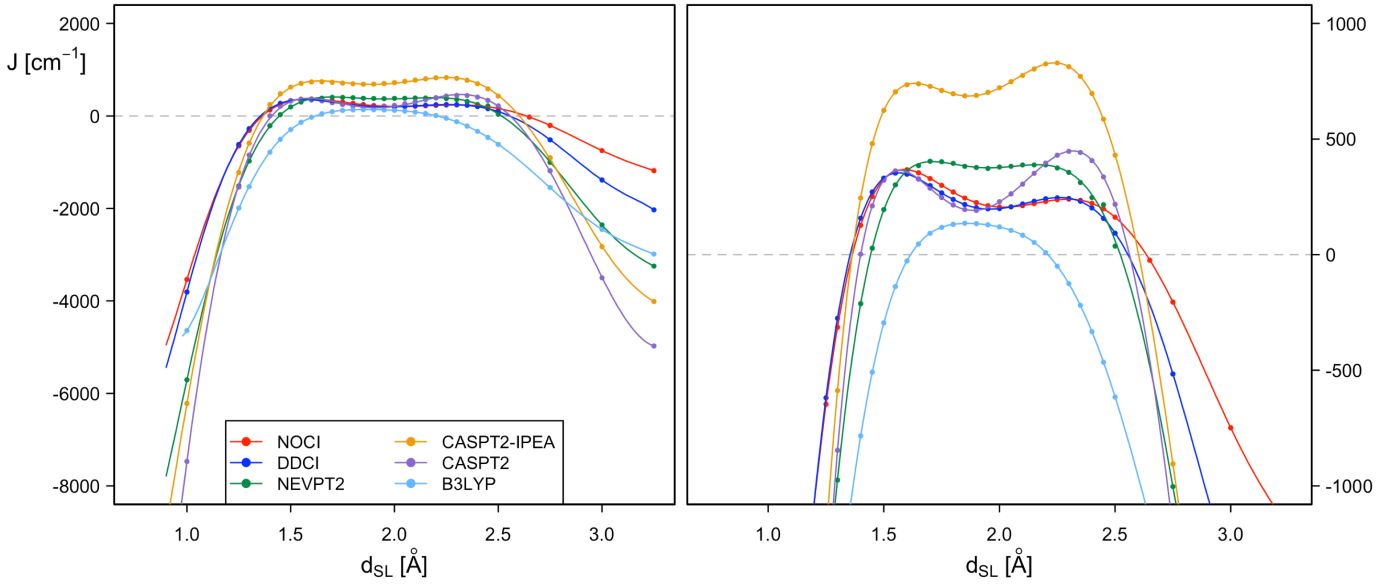

Fig. 4 Magnetic coupling between two PDTA molecules ($d_{IP} = 2.5$ Å) as function of the slippage along the x-axis (d_{SL}) calculated with different electronic structure methods.

range nature of dynamic correlation. The dressing of the wave function with dynamic correlation effects was done with the dynamic correlation dressed CAS (DCD-CAS) method, in which the coefficients of the CAS wave function are adapted in order to incorporate the effect of dynamic correlation. This revised wave function is then used to construct the MEBFs and the NOCI-F calculation proceeds as usual.

Shifting the MEBFs with the dynamic correlation correction only has a very small effect on the coupling between the different MEBFs. The $\langle S_1S_0|\hat{H}|^1TT\rangle$ coupling, relevant for the singlet fission efficiency, is small for all three tetracene pairs found in the experimental crystal structure and remains equally small after applying the dynamic correlation shift. However, the total coupling between the two states including the effect of the charge transfer configurations does change dramatically. Dynamic correlation stabilizes the charge transfer states, which makes that their contribution to the S_0S_1/S_1S_0 and ^1TT dominated NOCI wave functions increases. Therefore, the coupling with and without dynamic correlation are qualitatively different for two of the tetracene pairs. Although the dressing of the CAS wave function introduces subtle changes in the wave functions of the tetracene units, the couplings remain practically identical when the relative energies of the dressed and undressed MEBFs are made equal. This demonstrates that the changes in the wave function are small enough to not substantially change the couplings between the MEBFs, neither for the direct coupling nor for the total coupling after adding the effect of the CT configurations.

One of the advantages of NOCI-F is the fact that the final wave function is a very short expansion of well-defined electronic configurations. This makes the analysis of the wave function straightforward as illustrated for the diazadiborinine derivative studied here. The coefficients of the MEBFs can be used without any further processing to assign a label to the final NOCI states. Small differences in the relative importance of the MEBFs were observed for the BC dimer when the dynamic correlation shift was applied. A similar analysis of the CASSCF wave function requires either the generation of natural transition orbitals, which only capture one-electron replacements, or a tedious analysis of the very long CI expansion provided that the set of molecular orbitals lead to configuration state functions that are univocally identifiable, which might require orbital transformation to some set of localized orbitals.

NOCI has been applied some years ago to calculate magnetic coupling strengths, but at that time it was only possible to use MEBFs with only a few configurations and dynamic correlation could not be incorporated. In the present implementation these restrictions have been removed and here we demonstrated the capabilities of NOCI-F by calculating the magnetic coupling strength for two related organic radicals. The first conclusion that can be drawn is that NOCI-F reproduces very precisely the difference dedicated configuration interaction (DDCI) results at all the tested geometries. DDCI is considered to be the most accurate computational method for calculating isotropic magnetic coupling but requires CI expansions that can easily contain more than 10 million determinants, while the NOCI-F wave functions used here are expanded in less than ten MEBFs. Apart from the quantitative agreement with DDCI, NOCI-F also allows for a very simple analysis of the mechanisms that control the strength of the magnetic coupling: starting from the basic expansion using only the doublet ground state functions, one can gradually add local excited states and charge transfer states. Since these configurations are expressed in their own optimal orbital set there is no need to add relaxation effects, which were discussed at length by Calzado and co-workers[26,27,29] and form the basis for the success of DDCI. Other methods based on orthogonal MOs such as CASPT2 and NEVPT2 make use of internally contracted first-order wave functions, in which case special care needs to be taken to repair the underestimation of the importance of the ionic configurations before taking into account dynamic electron correlation as nicely illustrated in Refs. 29,88. This is not the case in the NOCI-F approach despite making use of precisely these methods to estimate the effect of dynamic electron correlation. This is because the NOCI-F follows a state specific approach in which neutral and ionic states are treated independently and the mixing between the two is only determined after the dynamic correlation correction has been applied for. The results presented here are promising, but need to be verified for other systems, especially the magnetic interactions in transition metal complexes. This is topic of ongoing studies.

Acknowledgements

This work used resources through the INCITE program of the Oak Ridge Leadership Computing Facility (OLCF) at the Oak Ridge National Laboratory, which is supported by the Office of Science of the U.S. Department of Energy under Contract No. DE-AC05-00OR22725. We acknowledge PRACE for awarding us access to JUWELS at GCS@FZJ, Germany. Financial support has been provided by the Spanish Ministerio de Ciencia Innovación y Universidades (Projects RTI2018-095460-B-I00, CTQ2017-83566-P, PID2020-113187GB-I00 and the Excellence María de Maeztu grant MDM-2017-0767) and by the Generalitat de Catalunya (Projects 2017SGR13 and 2017-SGR629). This work is part of the research program "Computational sciences for energy research" (project 15CSER73), which is financed by the Dutch Research Council (NWO). The data that supports the findings of this study are available within the article and its supplementary material. This manuscript has been authored in part by UT-Battelle, LLC, under contract DE-AC05-00OR22725 with the US Department of Energy (DOE). The US government retains and the publisher, by accepting the article for publication, acknowledges that the US government retains a nonexclusive, paid-up, irrevocable, worldwide license to publish or reproduce the published form of this manuscript, or allow others to do so, for US government purposes. DOE will provide public access to these results of federally sponsored research in accordance with the DOE Public Access Plan (http://energy.gov/downloads/doe-public-access-plan).

Notes and references

1 J. C. Johnson, A. J. Nozik and J. Michl, *Acc. Chem. Res.*, 2013, **46**, 1290–1299.

2 D. Casanova, *Chem. Rev.*, 2018, **118**, 7164–7207.

3 T. Jahnke, U. Hergenhahn, B. Winter, R. Dörner, U. Frühling,

P. V. Demekhin, K. Gokhberg, L. S. Cederbaum, A. Ehresmann, A. Knie and A. Dreuw, *Chem. Rev.*, 2020, **120**, 11295–11369.
4 O. V. Mikhnenko, P. W. M. Blom and T.-C. Nguyen, *Energy Environ. Sci.*, 2015, **8**, 1867–1888.
5 A. Bhunia, M. T. Gamer, L. Ungur, L. Chibotaru, A. K. Powell, Y. Lan, P. W. Roeski, F. Menges, C. Riehn and G. Niedner-Schatteburg, *Inorg. Chem.*, 2012, **51**, 9589–9597.
6 D. Gatteschi, R. Sessoli and F. Villain, *Molecular Nanomagnets*, Oxford University Press, Oxford, 2006.
7 M. Coey, M. Viret and S. von Molnár, *Adv. Phys.*, 1999, **48**, 167–293.
8 E. Dagotto, *Science*, 2005, **309**, 257–262.
9 C. J. Calzado, *Chem. Eur. J.*, 2012, **19**, 1254–1261.
10 S. N. Herringer, M. Deumal, J. Ribas-Ariño, J. J. Novoa, C. P. Landee, J. L. Wikaira and M. M. Turnbull, *Chem. Eur. J.*, 2014, **20**, 8355–8362.
11 J.-P. Malrieu, R. Caballol, C. J. Calzado, C. de Graaf and N. Guihéry, *Chem. Rev.*, 2014, **114**, 429–492.
12 C. de Graaf and R. Broer, *Magnetic Interactions in Molecules and Solids*, Springer, Heidelberg, 2015.
13 M. B. Smith and J. Michl, *Chem. Rev.*, 2010, **110**, 6891–6936.
14 B. Kaduk, T. Kowalczyk and T. Van Voorhis, *Chem. Rev.*, 2012, **112**, 321–370.
15 D. Casanova and M. Head-Gordon, *Phys. Chem. Chem. Phys.*, 2009, **11**, 9779–9790.
16 F. Bell, P. M. Zimmermann, D. Casanova, M. Goldey and M. Head-Gordon, *Phys. Chem. Chem. Phys.*, 2013, **15**, 358–366.
17 J. F. Stanton and J. Gauss, *Adv. Chem. Phys.*, 2003, **125**, 101–146.
18 A. I. Krylov, *Annu. Rev. Phys. Chem.*, 2008, **59**, 433–462.
19 S. Faraji, S. Matsika and A. I. Krylov, *J. Chem. Phys.*, 2018, **148**, 044103.
20 T. C. Berkelbach, M. S. Hybertsen and D. R. Reichman, *J. Chem. Phys.*, 2013, **138**, 114102.
21 C.-P. Hsu, *Acc. Chem. Res.*, 2008, **42**, 509–518.
22 C. M. Baronio and A. Barth, *J. Phys. Chem. B*, 2020, **124**, 1703–1714.
23 T. L. C. Jansen, *J. Chem. Phys.*, 2021, **155**, 170901.
24 J. Miralles, J.-P. Daudey and R. Caballol, *Chem. Phys. Lett.*, 1992, **198**, 555–562.
25 J. Miralles, O. Castell, R. Caballol and J.-P. Malrieu, *Chem. Phys.*, 1993, **172**, 33–43.
26 C. J. Calzado, J. Cabrero, J.-P. Malrieu and R. Caballol, *J. Chem. Phys.*, 2002, **116**, 2728–2747.
27 C. J. Calzado, J. Cabrero, J.-P. Malrieu and R. Caballol, *J. Chem. Phys.*, 2002, **116**, 3985–4000.
28 R. Bastardis, N. Guihéry and C. de Graaf, *Phys. Rev. B*, 2007, **76**, 132412.
29 C. J. Calzado, C. Angeli, D. Taratiel, R. Caballol and J.-P. Malrieu, *J. Chem. Phys.*, 2009, **131**, 044327.
30 M.-A. Bouammali, N. Suaud, R. Maurice and N. Guihéry, *J. Chem. Phys.*, 2021, **155**, 164305.
31 J.-P. Malrieu, P. Durand and J.-P. Daudey, *J. Phys. A*, 1985, **18**, 809–826.
32 T. P. Straatsma, R. Broer, S. Faraji, R. W. A. Havenith, L. E. Aguilar Suarez, R. K. Kathir, M. Wibowo and C. de Graaf, *J. Chem. Phys.*, 2020, **152**, 064111.
33 N. J. Mayhall, P. R. Horn, E. J. Sundstrom and M. Head-Gordon, *Phys. Chem. Chem. Phys.*, 2014, **16**, 22694–22705.
34 A. F. Morrison, Z.-Q. You and J. M. Herbert, *J. Chem. Theory Comput.*, 2014, **10**, 5366–5376.
35 J. Olsen, *J. Chem. Phys.*, 2015, **143**, 114102.
36 S. R. Yost and M. Head-Gordon, *J. Chem. Phys.*, 2016, **145**, 054105.
37 S. Kähler and J. Olsen, *J. Chem. Phys.*, 2017, **147**, 174106.
38 S. Kähler and J. Olsen, *J. Chem. Phys.*, 2018, **149**, 144104.
39 K. J. Oosterbaan, A. F. White and M. Head-Gordon, *J. Chem. Phys.*, 2018, **149**, 044116.
40 H. G. A. Burton, M. Gross and A. J. W. Thom, *J. Chem. Theory Comput.*, 2018, **14**, 607–618.
41 R. H. Myhre, *J. Chem. Phys.*, 2018, **148**, 094110.
42 S. R. Yost and M. Head-Gordon, *J. Chem. Theory Comput.*, 2018, **14**, 4791–4805.
43 K. J. Oosterbaan, A. F. White and M. Head-Gordon, *J. Chem. Theory Comput.*, 2019, **15**, 2966–2973.
44 I. O. Glebov, M. I. Kozlov and V. V. Poddubnyy, *Comput. Theor. Chem.*, 2019, **1153**, 12–18.
45 H. G. A. Burton and A. J. W. Thom, *J. Chem. Theory Comput.*, 2019, **15**, 4851–4861.
46 J. Nite and C. A. Jiménez-Hoyos, *J. Chem. Theory Comput.*, 2019, **15**, 5343–5351.
47 C. Stinson, *PhD thesis*, University of Canterbury, Christchurch, New Zealand, 2020.
48 H. G. A. Burton and A. J. W. Thom, *J. Chem. Theory Comput.*, 2020, **16**, 5586–5600.
49 T. P. Straatsma, R. Broer, S. Faraji and R. W. A. Havenith, *Annu. Rep. Comp. Chem.*, 2018, **14**, 77–91.
50 R. K. Kathir, C. de Graaf, R. Broer and R. W. A. Havenith, *J. Chem. Theory Comput.*, 2020, **16**, 2941–2951.
51 M. Wibowo, R. Broer and R. W. A. Havenith, *Comput. Theor. Chem.*, 2017, **1116**, 190–194.
52 J. L. Ryerson, A. Zaykov, L. E. Aguilar Suarez, R. W. A. Havenith, B. R. Stepp, P. I. Dron, J. Kaleta, A. Akdag, S. J. Teat, T. F. Magnera, J. R. Miller, Z. Havlas, R. Broer, S. Faraji, J. Michl and J. C. Johnson, *J. Chem. Phys.*, 2019, **151**, 184903.
53 A. Zaykov, P. Felkel, E. A. Buchanan, M. Jovamovic, R. W. A. Havenith, R. K. Kathir, R. Broer, Z. Havlas and J. Michl, *J. Am. Chem. Soc.*, 2019, **141**, 17729–17743.
54 L. E. Aguilar Suarez, R. K. Kathir, E. Siagri, R. W. A. Havenith and S. Faraji, *Adv. Quantum Chem.*, 2019, **79**, 263–287.
55 L. E. Aguilar Suarez, C. de Graaf and S. Faraji, *Phys. Chem. Chem. Phys.*, 2021, **23**, 14164–14177.
56 S. Pathak, L. Lang and F. Neese, *J. Chem. Phys.*, 2017, **147**, 234109.

57 F. Neese, F. Wennmohs, U. Becker and C. Riplinger, *J. Chem. Phys.*, 2020, **152**, 224108.

58 E. Pradhan, J. N. Bentley, C. B. Caputo and T. Zeng, *ChemPhotoChem*, 2020, **4**, 5279–5287.

59 R. Broer and W. C. Nieuwpoort, *Chem. Phys.*, 1981, **54**, 291–303.

60 R. Broer and W. C. Nieuwpoort, *Theor. Chim. Acta*, 1988, **73**, 405–418.

61 P.-O. Löwdin, *J. Chem. Phys.*, 1950, **18**, 365–375.

62 C. de Graaf, R. Broer, W. C. Nieuwpoort and P. S. Bagus, *Chem. Phys. Lett.*, 1997, **272**, 341–346.

63 A. H. de Vries, L. Hozoi, R. Broer and P. S. Bagus, *Phys. Rev. B*, 2002, **66**, 035108.

64 L. Hozoi, A. H. de Vries, R. Broer, C. de Graaf and P. S. Bagus, *Chem. Phys.*, 2006, **331**, 178–185.

65 A. B. van Oosten, R. Broer and W. C. Nieuwpoort, *Chem. Phys. Lett.*, 1996, **257**, 207–212.

66 A. B. van Oosten and F. Mila, *Chem. Phys. Lett.*, 1998, **295**, 359–365.

67 A. Stoyanova, C. Sousa, C. de Graaf and R. Broer, *Int. J. Quantum Chem.*, 2006, **106**, 2444–2457.

68 C. Angeli, R. Cimiraglia, S. Evangelisti, T. Leininger and J.-P. Malrieu, *J. Chem. Phys.*, 2001, **114**, 10252–10264.

69 J. P. Zobel, J. J. Nogueira and L. González, *Chem. Sci.*, 2016, **8**, 1482–1499.

70 K. Pierloot, Q. M. Phung and A. Domingo, *J. Chem. Theory Comput.*, 2017, **13**, 537.

71 C. Kollmar, K. Sivalingam and F. Neese, *J. Chem. Phys.*, 2020, **152**, 214110.

72 R. Sarkar, P.-F. Loos, M. Boggio-Pasqua and D. Jacquemin, *J. Chem. Theory Comput.*, 2022, **in press**, doi.org/10.1021/acs.jctc.1c01197.

73 R. K. Kathir, *PhD thesis*, University of Groningen, 2022.

74 G. A. Gallup and J. M. Norbeck, *Chem. Phys. Lett.*, 1973, **21**, 495–500.

75 K. G. Dyall, *J. Chem. Phys.*, 1995, **102**, 4909–4918.

76 F. Aquilante, J. Autschbach, A. Baiardi, S. Battaglia, A. C. Borin, L. Chibotaru, I. Conti, L. De Vico, M. Delcey, I. Fernández-Galván, N. Ferré, L. Freitag, M. Garavelli, X. Gong, S. Knecht, E. D. Larsson, R. Lindh, M. Lundberg, P.-Å. Malmqvist, A. Nenov, J. Norell, M. Odelius, M. Olivucci, T. B. Pedersen, L. Pedraza-González, Q. M. Phung, K. Pierloot, M. Reiher, I. Schapiro, J. Segarra-Martí, F. Segatta, L. Seijo, S. Sen, D.-C. Sergentu, C. J. Stein, L. Ungur, M. Vacher, A. Valentini and V. Veryazov, *J. Chem. Phys.*, 2020, **152**, 214117.

77 R. B. Campbell, J. M. Robertson and J. Trotter, *Acta Crystallogr.*, 1962, **15**, 289–290.

78 B. Wang, Y. Li, R. Ganguly, H. Hirao and R. Kinjo, *Nature Comm.*, 2016, **7**, 11871.

79 R. Dovesi, A. Erba, R. Orlando, C. M. Zicovich-Wilson, B. Civalleri, L. Maschio, M. Rérat, S. Casassa, J. Baima, S. Salustro and B. Kirtman, *WIREs Comput. Mol. Sci.*, 2018, **8**, el1360.

80 T. Francese, J. Ribas-Ariño, J. J. Novoa, R. W. A. Havenith, R. Broer, C. de Graaf and M. Deumal, *Phys. Chem. Chem. Phys.*, 2018, **20**, 20406.

81 A. Alberola, R. J. Collis, S. M. Humphrey, R. J. Less and J. M. Rawson, *Inorg. Chem.*, 2006, **45**, 1903–1905.

82 B. O. Roos, R. Lindh, P.-Å. Malmqvist, V. Veryazov and P.-O. Widmark, *J. Phys. Chem. A*, 2004, **108**, 2851–2858.

83 S. A. Bäppler, F. Plasser, M. Wormit and A. Dreuw, *Phys. Rev. A*, 2014, **90**, 052521.

84 F. Plasser, M. Wormit and A. Dreuw, *J. Chem. Phys.*, 2014, **141**, 024106.

85 S. Vela, M. B. Reardon, C. E. Jakobsche, M. M. Turnbull, J. Ribas-Arino and J. J. Novoa, *Chem. Eur. J.*, 2017, **23**, 3479–3489.

86 N. Queralt, D. Taratiel, C. de Graaf, R. Caballol, R. Cimiraglia and C. Angeli, *J. Comput. Chem.*, 2008, **29**, 994–1003.

87 C. Angeli, R. Cimiraglia and J.-P. Malrieu, *Chem. Phys. Lett.*, 2001, **350**, 297–305.

88 C. Angeli, C. J. Calzado, R. Cimiraglia and J.-P. Malrieu, *J. Chem. Phys.*, 2006, **124**, 234109.